

Unseeded molecular flow tagging in cold and hot flows using ozone and hydroxyl tagging velocimetry

Robert W Pitz[†], Joseph A Wehrmeyer[†], Lubomir A Ribarov[†],
Douglas A Oguss[†], Farrokh Batliwala[†], Peter A DeBarber[‡],
Stefan Deusch[§] and Paul E Dimotakis[§]

[†] Department of Mechanical Engineering, Vanderbilt University, Nashville, TN 37235, USA

[‡] MetroLaser, Inc, Irvine, CA 92614, USA

[§] Graduate Aeronautical Laboratories, California Institute of Technology, Pasadena, CA 91125, USA

Received 13 January 2000, in final form and accepted for publication 4 May 2000

Abstract. Two complementary unseeded molecular flow tagging techniques for gas-flow velocity field measurement at low and high temperature are demonstrated. Ozone tagging velocimetry (OTV) is applicable to low-temperature air flows whereas hydroxyl tagging velocimetry (HTV) is amenable to use in high-temperature reacting flows containing water vapour. In OTV, a grid of ozone lines is created by photodissociation of O₂ by a narrowband 193 nm ArF excimer laser. After a fixed time delay, the ozone grid is imaged with a narrowband KrF laser sheet that photodissociates the ozone and produces vibrationally excited O₂ that is subsequently made to fluoresce by the same KrF laser light sheet via the O₂ transition B³Σ_u⁻ (v' = 0, 2) ← X³Σ_g⁻ (v'' = 6, 7). In HTV, a molecular grid of hydroxyl (OH) radicals is written into a flame by single-photon photodissociation of vibrationally excited H₂O by a 193 nm ArF excimer laser. After displacement, the OH tag line position is revealed through fluorescence caused by OH A²Σ⁺ ← X²Π (3 ← 0) excitation using a 248 nm tunable KrF excimer laser. OTV and HTV use the same lasers and can simultaneously measure velocities in low and high temperature regions. Instantaneous flow-tagging grids are measured in air flows and a flame. The velocity field is extracted from OTV images in an air jet using the image correlation velocimetry (ICV) method.

Keywords: laser diagnostics, molecular flow tagging, fluid flow velocity, excimer lasers, combustion diagnostics, image correlation velocimetry

1. Introduction

Most quantitative laser-based methods for gas flow velocity measurements are based on scattering of light from particles seeded in the gas flow. Laser-Doppler anemometry and particle imaging velocimetry (PIV) are two widely used, commercially available systems [1, 2]. With the large light-scattering cross-section of particles, particle-based methods can provide very accurate velocity measurements. However, in high-speed flows, the particle seed does not always track the gas velocity and particle-seeding methods can give gross errors. Also, the addition of particle seeds into large test facilities can be detrimental to the facility. Velocimetry methods, with no particle seeding, that measure the Lagrangian velocity of fluid parcels, can be preferable.

Molecular-based velocimetry methods based on measuring the Doppler shift of light scattered from a molecular tracer have been developed [3]. In laser-induced fluorescence methods, Doppler shifts of sodium [4], iodine [5] and nitric oxide [6] have been measured to determine gas flow velocity. The

Doppler shift of Rayleigh-scattered laser light has been measured with Fabry–Pérot interferometers and molecular filters to give the velocity field [7, 8]. Doppler shift methods are often used in high-speed flows but are inaccurate at low velocities because the Doppler shift is extremely small.

Molecular tagging methods are potentially able to track both low and high velocities. In these methods, a molecular marker is written into the gas and velocity is determined by measuring the displacement of the marker over time. Several molecular tagging methods that rely on molecular seeding of the gas flow have been developed. Laser-induced phosphorescence of biacetyl lines was used for the visualization of nitrogen flows [9, 10]. Since oxygen quenches the phosphorescence of biacetyl, flow tagging measurements using biacetyl have been limited to nitrogen flows. NO grids have recently been written in gas flows by seeding the flow with NO₂ [11]. Molecular tagging methods involving seeding are often undesirable. The molecular seed can be toxic or environmentally hazardous. Furthermore, it is often difficult to distribute the seeding throughout the flow.

Several time-of-flight molecular-flow tagging velocity measurement techniques that do not require seeding have been developed. The first methods were based on nonlinear optical processes, resulting in relatively short tag lines. In two-photon photodissociation of water vapour (H₂O), a KrF excimer laser operating at 248 nm produces a 1.5 mm tag line of the hydroxyl radical (OH) and is subsequently fluoresced to profile the flow velocity [12]. In the Raman excitation plus laser-induced electronic fluorescence (RELIEF) method, a nonlinear stimulated Raman process produces a roughly 10 mm long tag line of vibrationally excited oxygen (O₂) whose enhanced fluorescence excitation strength (over that of ground-state O₂) reveals the displacement of the tag when the flowfield is subsequently irradiated by an ultraviolet (UV) laser [13].

Unseeded molecular tagging methods based on single-photon processes that can produce long lines have recently been developed. In ozone tagging velocimetry (OTV), a line of ozone (O₃) is produced by a single photon from a 193 nm ArF excimer laser. After a time delay, a second laser pulse reveals the displaced O₃ tag line position by causing photodissociation of O₃ and subsequent fluorescence of the vibrationally excited O₂ photoproduct. Use of the OTV technique in low-temperature air flows, writing as many as six intersecting lines of 20–40 mm length, has been described and demonstrated [14–17]. The OTV method is well suited for low-temperature flows; however, at high temperatures, both the tag line lifetime and the peak concentration of O₃ are reduced [15–17]. Therefore, hydroxyl tagging velocimetry (HTV) has been developed for use in high-temperature reacting flows [17, 18]. In HTV, a single 193 nm photon dissociates vibrationally hot water vapour into OH and H. The OH line or grid is revealed by OH fluorescence induced by a 248 nm KrF excimer laser.

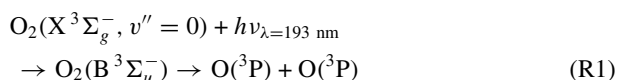
This paper describes the OTV and HTV techniques and recent advances allowing one to produce more grid lines with a better signal-to-noise ratio. In addition, image correlation velocimetry (ICV) [19] is applied to analyse the displacement of the OTV grids in order to produce quantitative velocity fields.

2. OTV

2.1. OTV photochemistry

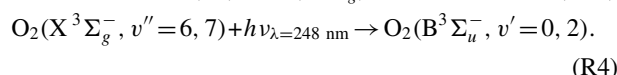
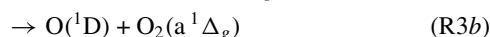
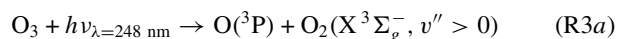
A conceptual drawing of the OTV technique is shown in figure 1. First a tag line of O₃ is created from O₂ by a pulsed argon-fluoride (ArF) excimer laser operating at ≈ 193 nm. After a known delay time, τ , the position of the O₃ tag line is revealed by photodissociation of O₃ and subsequent fluorescence of O₂, both caused by a pulsed laser sheet from a krypton-fluoride (KrF) excimer laser operating at ≈ 248 nm. Camera images of the fluorescence from the initial and final line locations provide means for establishing a velocity profile.

The O₃ line or grid is ‘written’ by two sequential reactions:



In reaction (R1), a single photon of 193 nm light excites ground-state O₂ to the predissociative state O₂ (B³Σ_u⁻) that rapidly decomposes (at a rate of $\approx 10^{11}$ s⁻¹ [16]) into ground state ({}³P) oxygen atoms. The rate of formation of ozone is governed by a three-body reaction (R2) that is slow relative to (R1). For M = N₂ the rate constant of the reaction is $k_2 = 5.7 \times 10^{-46}$ m⁶ s⁻¹ under standard conditions [20]. With this rate constant, the time of formation of $\approx 63\%$ of the steady-state O₃ concentration (at STP) is $1/(k_2 n_{\text{O}_2} n_{\text{N}_2}) \approx 20$ μs, where n is the number density.

The displaced O₃ line is ‘read’ by the 248 nm light sheet through reactions (R3a) and (R4):



In reaction (R3), O₃ is efficiently dissociated by the KrF laser. The 248 nm light is in the Hartley absorption band that occurs from 245 to 265 nm [21]. With an absorption cross-section of approximately 10⁻¹⁷ cm² per molecule and 248 nm laser fluences of the order of 4 J cm⁻², it is expected that all of the O₃ will be photodissociated by a single laser pulse. However, O atoms from the dissociation could reform O₃, which was suggested in an earlier work [14], in which multiple reads of an ozone ribbon were accomplished.

Reaction (R3) leads to two sets of photoproducts. Only the vibrationally excited O₂ (X³Σ_g⁻, v'' = 6, 7) photoproduct can be fluoresced by the 248 nm ‘read’ laser. About 6–15% of the ozone decomposes to vibrationally excited O₂ (R3a) for 248 nm excitation [22]. The excited O₂ molecules have a distribution of vibrational quantum numbers with a maximum near the v'' = 6 and 7 levels [23]. These levels can be directly fluoresced by the 248 nm excimer ‘read’ laser. Experimentally, it is determined that pumping the (v' = 0 ← v'' = 6) vibrational transition is the most efficient in terms of producing detectable fluorescence [16].

2.2. The chemistry of generation and destruction of ozone tag lines

The rates of formation and destruction of ozone are important for the applicability of OTV to air flows at various temperatures and pressures. Velocity measurements in a variety of laboratory and test facilities in which thermodynamic conditions vary and contaminants (e.g. water and nitric oxide) are present are needed. To predict the concentration of O₃ as a function of temperature, pressure and time, the CHEMKIN II thermodynamic database and the SENKIN chemical kinetics solver [24] are used with a set of 119 reversible reactions, including reactions involving nitrogen oxides [17].

Ozone concentration levels in three different environments, namely dry air, humid air and polluted humid air, were calculated as a function of time (see figure 2). In the case of dry air, the initial mole fractions of N₂ and O₂ are 79.00 and 20.79% respectively. Here it is assumed that $\approx 1\%$ of the O₂ molecules are photodissociated into O atoms by the ArF laser. About 1% dissociation of the ambient O₂ is

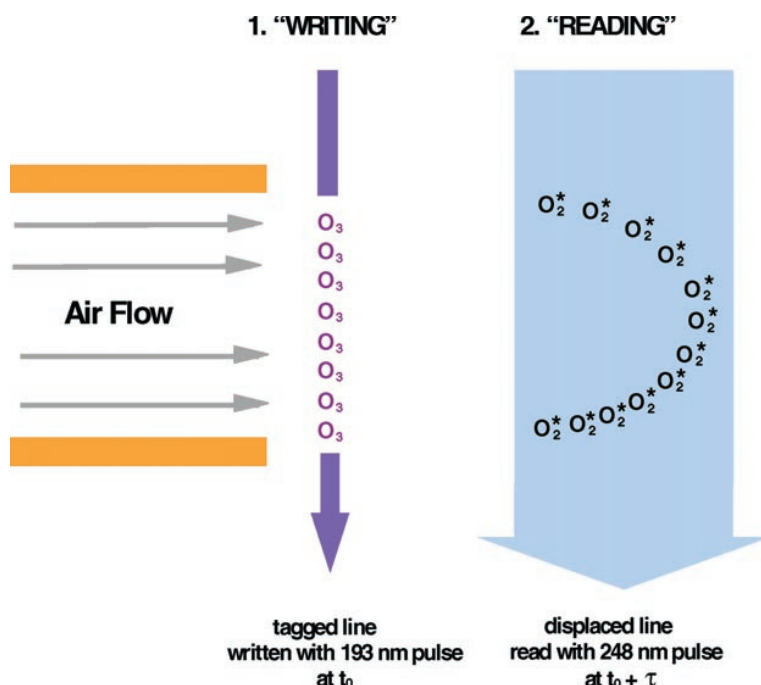


Figure 1. A conceptual diagram showing OTV for a convective velocity profile of a Hagen–Poiseuille-type flow.

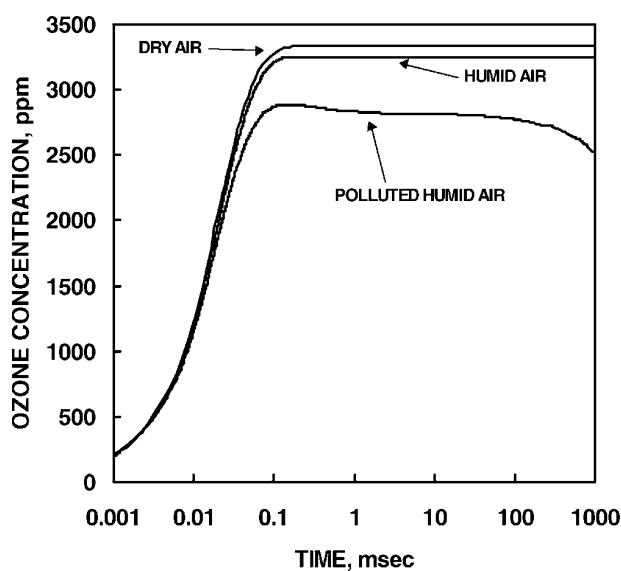
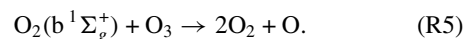


Figure 2. O_3 concentration versus time for dry air, humid air and humid air with 100 ppm NO. All three cases are at 1 atm and an initial temperature of 300 K.

expected for typical OTV conditions (10 mJ per 300 μm diameter beam in the OTV grid), such as when the laser is tuned to the P (17) line at 193.293 nm with $0.03 \text{ cm}^{-1} \text{ atm}^{-1}$ absorption [25].

For 1% dissociation of O_2 at 300 K and 1 atm, the estimated initial O atom concentration is 4200 ppm (by volume (ppm(v))). If all the O atoms formed O_3 , one would expect a steady-state concentration of O_3 of 4200 ppm(v). As can be seen in figure 2, a slightly lower steady-state O_3 concentration of ≈ 3300 ppm(v) is predicted to occur after ≈ 1 ms. To determine the cause of this ozone deficit, the reactions for formation and destruction of ozone are analysed

with the SENKIN code. As can be seen in figure 3, the concentration of ozone is depleted by the following reaction of ozone with singlet molecular oxygen, ($O_2(b^1\Sigma_g^+)$):



That reaction (R2) controls the formation of O_3 is confirmed by the high rate of production of O_3 seen in figure 3. As can be seen in figure 2, the O_3 concentration rises rapidly, attaining over 50% of its steady-state value within 20 μs .

In the humid air case (3.5% mole fraction of water at 300 K), the steady-state O_3 concentrations are lower (figure 2). The slight drop in steady-state O_3 concentration for the humid air is due to the initial O_2 concentration being lower (still assuming 1% dissociation of the O_2) and the O atom concentration being concomitantly lower. The addition of 3.5% mole fraction of water vapour has no chemical effect on the O_3 concentration.

Polluted humid air is modelled by the addition of 100 ppm(v) of NO to the humid air. As can be seen in figure 4, NO efficiently removes O_3 by the following well-known reaction, which is important in tropospheric pollution modelling [21]:



The other two NO reactions shown in figure 4 are less important and lead to a slight nett production of O_3 . The results of figure 2 are all for an initial temperature of 300 K and a slight rise in temperature (≈ 30 K) occurs as a result of the initial laser absorption that dissociates O_2 and subsequently causes release of heat in formation of O_3 from O and O_2 .

Effects of pressure and temperature on the lifetime of ozone are shown in figure 5. At these higher temperatures

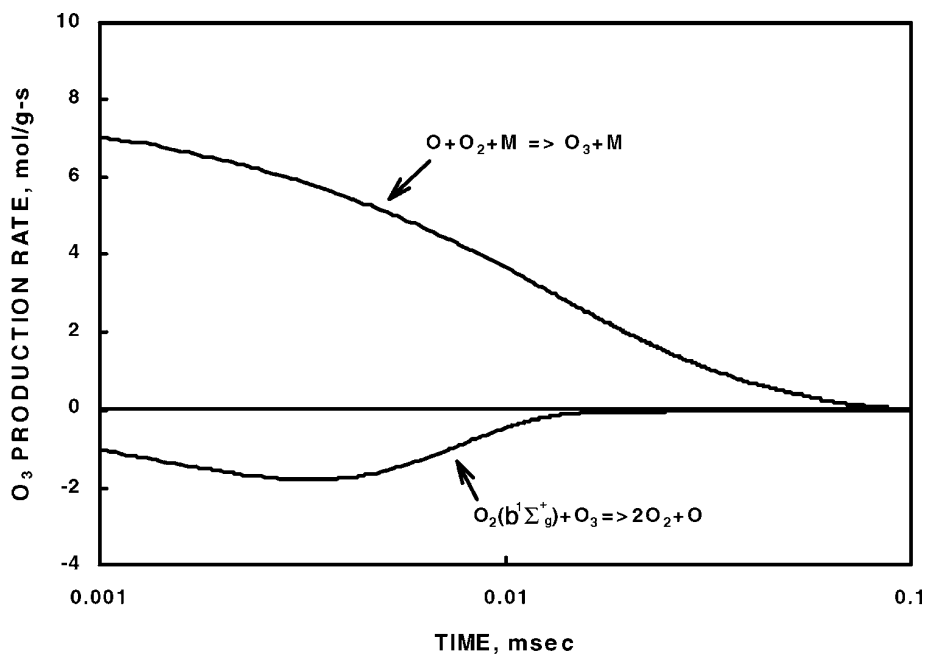


Figure 3. Rates of production and destruction of ozone for the polluted humid air simulation shown in figure 2 at 300 K and 1 atm.

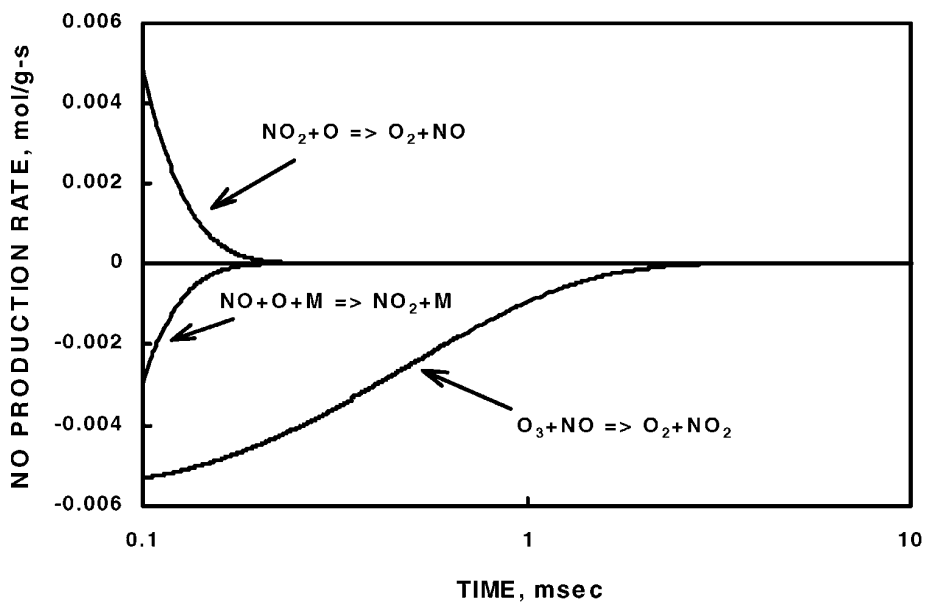


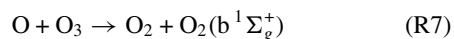
Figure 4. Rates of production and destruction of NO for the polluted humid air simulation shown in figure 2 at 300 K and 1 atm.

(500–600 K), the ozone tag persists for about 1 ms. The shorter lifetime of O₃ is not a serious issue in the application of OTV to flows at elevated temperature, since delay times between write and read laser pulses typically range from 20 μs to 2 ms for high-speed and low-speed flows, respectively.

Higher temperatures do have a detrimental effect on the maximum ozone concentration. For atmospheric pressure and 600 K, the maximum ozone concentration is only 200 ppm(v), less than a tenth of the value at 300 K. This drop in peak O₃ concentration is problematic since the read laser produces less fluorescence signal as a result of the lower populations of O₃ and vibrationally excited O₂. Thus, OTV

measurements will be increasingly difficult for temperatures above 600 K.

The important formation and destruction reactions were analysed for the higher temperature case of 600 K and 1 atm (see figure 6). The major formation reaction remains reaction (R2). For times less than 0.1 ms, reaction (R5) is still the major depleting reaction. After about 0.08 ms, two other reactions lead to destruction of ozone:



After about 2 ms (not shown in figure 6), reaction (R2) reverses and is the dominant route for destruction of ozone.

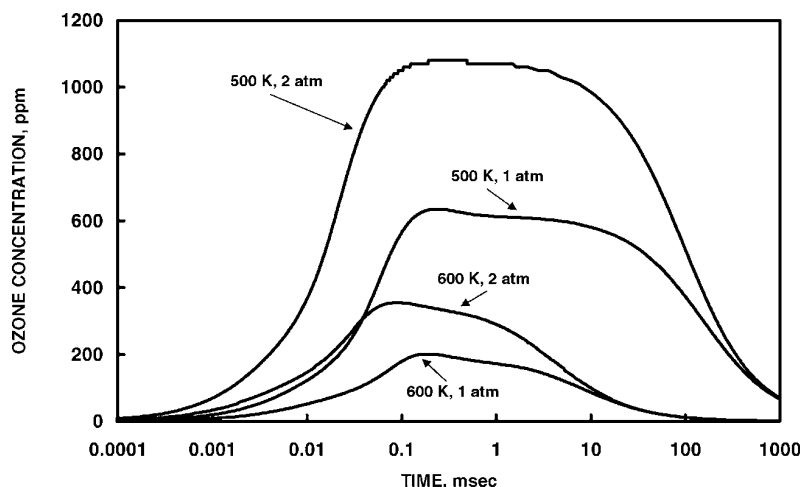


Figure 5. O_3 concentration versus time for dry air for several pressure and temperature conditions.

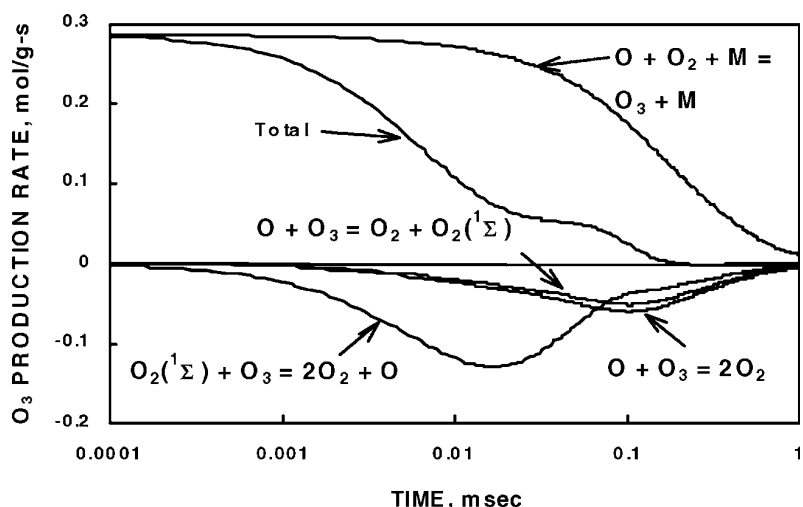


Figure 6. Rates of production and destruction of ozone for the high-temperature air simulation shown in figure 5 at 600 K and 1 atm.

Reactions (R5), (R7) and (R8) also contribute to depletion of ozone after 2 ms.

For times less than 2 ms, the O_3 is produced by a termolecular reaction (R2) while it is destroyed by bimolecular collisions ((R5), (R7) and (R8)). Since termolecular reaction rates scale as P^2 and bi-molecular reactions scale as P , the rate of production of O_3 relative to the rate of its destruction increases linearly with pressure. As can be seen in figure 5, doubling the pressure in the simulation leads to an increase by about a factor of two in maximum O_3 concentration.

2.3. OTV multi-line imaging

A sketch of the multi-line OTV set-up is shown in figure 7. The 193 nm output from a narrowband ArF excimer laser (150 mJ per pulse, tunable, 0.003 nm linewidth) is split into two beams that are crossed in the flowfield. The ArF beams are each focused to a 0.5 mm beam waist by a 1 m lens with fluences of the order of 20 J cm^{-2} . The total distance travelled by the ArF beams is about 2 m, leading to a loss of about half of the beam energy. The 248 nm output from a narrowband

KrF laser (400 mJ per pulse, tunable, 0.001 nm linewidth) is focused by a 1 m cylindrical lens to a sheet 20 mm by 0.5 mm in the flowfield. Light from the flowfield is recorded by a Princeton Instruments ICCD camera (576×384 pixels) using a UV lens ($f/4.5$ Nikkor). A butyl acetate filter (a low pass filter at 255 nm) in front of the camera lens blocks the laser radiation from both UV lasers but passes the O_2 fluorescence produced by the KrF read laser.

An instantaneous OTV image obtained using the two-line OTV system is shown in figure 8. The flowfield is a straight nozzle (27 mm diameter) of air excited by an acoustic speaker. A square-wave oscillation (1 Hz) drives the speaker and produces the 'mushroom'-shaped vortex shown in figure 8. The original positions of the lines (shown by the broken lines in figure 8) are marked by reading the OTV image at 0 ms. The mushroom vortex was recorded 4 ms after the lines had been written. The long delay between the read and write steps demonstrates the long life of the ozone tag in the 294 K air flow. Measurements were performed ≈ 15 mm downstream from the nozzle's exit. The velocity at the crossing point is 2 m s^{-1} , demonstrating the ability of OTV to measure low-velocity flows.

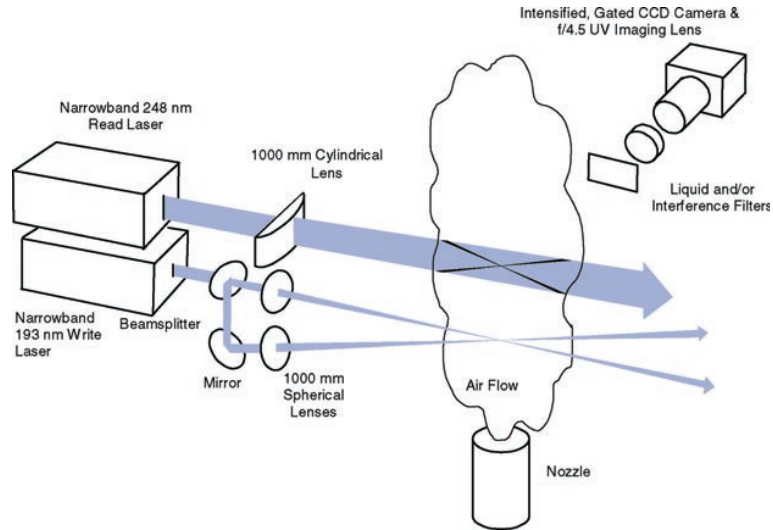


Figure 7. The experimental set-up for the OTV method based on two tunable excimer lasers.

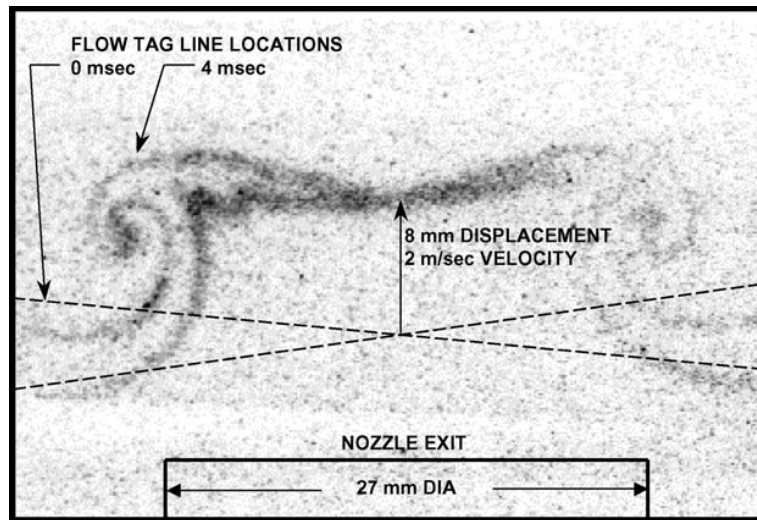


Figure 8. An instantaneous OTV image of a vortex flow of dry air under nearly standard conditions, exiting from a nozzle attached to a loudspeaker receiving a 1 Hz square-wave signal.

Furthermore, the OTV system was improved to form a 3×3 grid. The 248 nm output from a narrowband KrF laser (400 mJ per pulse, tunable, 0.001 nm linewidth) is focused by a 1 m cylindrical lens to a sheet 7 mm by 0.5 mm (fluences of the order of 10 J cm^{-2}) in the flowfield. The ArF laser was split into six beams. A 500 mm lens focused each beam to ≈ 0.3 mm diameter in the flowfield. To obtain a better signal-to-noise ratio the butyl acetate filter was replaced by a Schott WG305 2 mm thick glass filter. Instantaneous OTV images were taken from a 12.5 mm nozzle with a flowrate of 20 slpm, yielding a nozzle exit velocity of $\approx 2.5 \text{ m s}^{-1}$. Figure 9(a) shows the undisplaced grid (0 ms) and figure 9(b) shows the displaced grid ($\tau = 1$ ms). The flow is proceeding from the upper left-hand corner to the lower right-hand corner in each figure. Measurements were performed ≈ 25 diameters downstream from the exit of the nozzle.

2.4. Velocity field ICV from OTV data

The pair of OTV images shown in figure 9 and separated by a time τ was processed to infer the convecting velocity field in the image plane, assuming that image contrast captures a passive, non-diffusive, Lagrangian field. The convecting velocity was estimated using ICV [19]. The passive scalar transport property can be used to find an optimal displacement field $\xi(x)$ required to map an image $I_1(x)$, at t_1 , onto an image $I_2(x)$, at $t_2 = t_1 + \tau$, by correlation of their grey values. This can be formulated as the minimization of a least-squares cost function, $J(\xi)$, over a specified correlation domain Ω , i.e.

$$J\{\xi\} = \int_{\Omega} [I_2(x + \xi, t_1 + \tau) - I_1(x, t_1)]^2 d\Omega \rightarrow \min. \quad (1)$$

The optimized displacement field, $\xi(x)$, represents the maximum-likelihood solution to the image-correlation problem with respect to the velocity (displacement) field (point-to-point mapping) over the selected, two-dimensional domain, Ω [19].

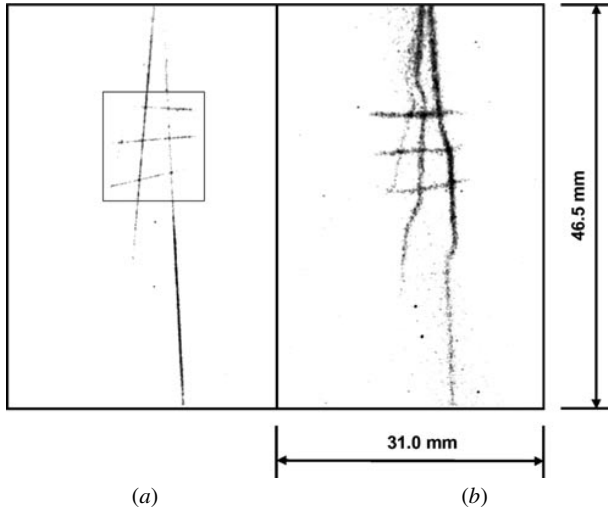


Figure 9. Instantaneous 3×3 OTV grid images in air flow from a 12.5 mm diameter jet. Write/read delays are (a) 0 ms and (b) $\tau = 1$ ms. The variational domain, Ω , is indicated by the rectangular region in a.

The solution of the variational problem, for short time intervals, corresponds to the leading-order equation

$$\tau \frac{\partial}{\partial t} I_1(x, t) + \xi \cdot \frac{\partial}{\partial x} I_1(x, t) \cong 0 \quad (2)$$

which is recognized as the scalar-transport equation if diffusion during the time interval τ may be assumed negligible. ICV can process images of particles, dye, gas-phase markers, such as in OTV, or any Lagrangian marker as long as the image has finite grey-value gradients (which is necessary in order to make the transport equation invertible for $\xi(x)$ for any optical method).

In its current implementation [26], a compact representation of the continuous advection field, $\xi(x)$, is written in terms of a Cartesian-product B -spline surface [27], i.e. a tensor product of bi-variate basis functions in x and y , weighted by local geometrical coefficients. The bi-variate basis functions are defined over a two-directional net of control points (two orthogonal knot vectors),

$$\xi(x) = \sum_i \sum_j p_{ij} B_i(x) B_j(y). \quad (3)$$

The geometrical coefficients, p_{ij} , permit a parametric description of the displacement field, $\xi(x)$, rendering the variational problem finite-dimensional. The properties of B -spline surfaces (in two and three dimensions) follow from the properties of B -spline curves [27]. B -splines are invariant with respect to affine transformations, have compact support and are piecewise polynomial functions of degree n . For a certain degree n and a given knot-vector grid, all property-defining basis functions follow.

Continuity and differentiability also follow from the basis functions. The B -spline curve is at least C^{n-s} -continuous, where s equals the multiplicity of the knot. The type of knot vector implemented was a uniform, non-periodic (clamped or open) knot vector, with equally spaced knots in the interior and $(n + 1)$ multiple knots at the

endpoints. The latter condition enforces the endpoint-interpolating property of the curve. Since solutions of the Navier–Stokes equation are C^∞ -continuous, implementation of a global $\xi(x)$ with at least C^{n-1} -continuity is an important advantage in representing real velocity fields.

Characteristics of the B -spline grid are user-specified. In particular, a hierarchy of superposed B -spline grids can be used to accommodate a locally variable spatial resolution. The B -spline basis-function order n can also be chosen, e.g. $n = 1$ (linear), $n = 2$ (quadratic), $n = 3$ (cubic), etc as required. B -splines are polynomial and, if they are of sufficiently high order, velocity derivatives (e.g. vorticity, rate-of-strain, Laplacian, etc) can be computed analytically.

Expressing the displacement field, $\xi(x)$, parametrically in terms of B -splines converts the functional, $J\{\xi\}$, into a function, $J[\xi(x; p)]$, where $p = (p_1, p_2, \dots, p_N)$ is the B -spline parameter list, with $\partial J[\xi(x; p)] / \partial p_i = 0$, for all i , at the multidimensional solution point, $p = p^*$. The velocity field is then approximated by $u(x, t + \tau/2) = \xi(x; p^*) / \tau$. ICV can be used in combination with other methods. The mapping (displacement) field, $\xi(x)$, can be initialized using cross-correlation over a patch grid, as in digital PIV, for example, even though not necessarily so.

The OTV image pair processed as described above is reproduced in figure 9. The scalar field to be tracked is comprised of two sets of three fluorescent (excited oxygen) lines. The rectangle in the image in figure 9(b) denotes the domain, Ω , used in minimizing the cost function, $J[\xi(x; p)]$.

Three sample results are depicted in figure 10, for three choices of B -spline grid (spatial resolution) and B -spline order. In each of the three images, the inferred velocity field in Ω is plotted over the (faint) pair of input images that are superimposed. In the image on the left-hand side, the ξ -field is described with a single, Ω -sized patch, using bilinear B -splines, i.e. with a total of $N = d P_x P_y = 8$ parameters, where $d = 2$ is the dimension and $P_x = P_y = 2$ is the number of support points in each direction. The value of the minimized cost function in this case is $J^*/J_0 = 0.528$, where J_0 is the initial value of the cost function. In the centre image, the ξ -field is described with a single patch and biquadratic B -splines, i.e. with $N = 18$ parameters ($d = 2$ and $P_x = P_y = 3$), with $J^*/J_0 = 0.495$. Note the quadratic (versus linear) variation of the velocity in the top row. Finally, in the image on the right-hand side, 2×2 biquadratic B -spline patches were used, i.e. $N = 32$ parameters ($d = 2$ and $P_x = P_y = 4$), yielding $J^*/J_0 = 0.417$. The effect of the higher spatial resolution in the inferred field is evident. Lower-resolution ICV patches act, in effect, as low-pass filters on the true velocity field.

The primary information in the image data is carried by the $9 = 3 \times 3$ intersections of the OTV lines, i.e. $M = 9d = 18$ coordinate values. The velocity field in the left-hand image was computed by determining $N < M$ parameters. The one in the centre with $N = M$ parameters may well be the most reliable of the three. The velocity field on the right-hand side, however, resulted from allowing $N > M$ parameters to be determined; the data most probably contain insufficient information to warrant such a representation. Although further increases in the number of B -spline patches, or in the order, would yield lower $J(\xi)$ values, they would

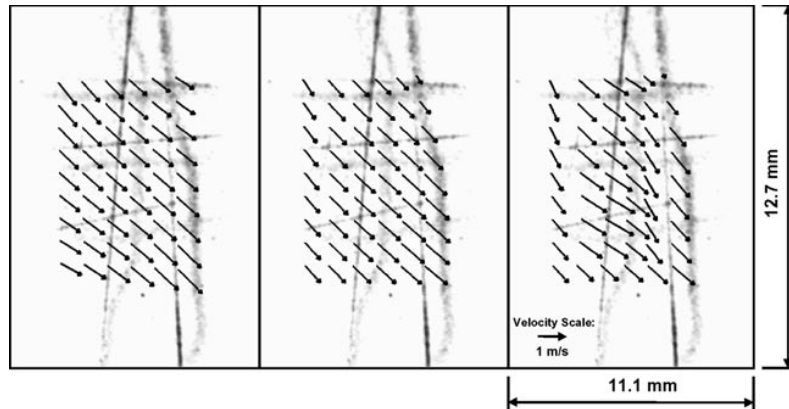


Figure 10. Three examples of inferred velocity fields, plotted over the mapping domain, Ω . Left-hand image: a single bilinear B -spline patch covering Ω ($J^*/J_0 = 0.528$). Centre: a single biquadratic patch ($J^*/J_0 = 0.495$). Right-hand image: 2×2 biquadratic patches ($J^*/J_0 = 0.417$).

do so at the expense of producing spurious features in the inferred $\xi(x)$ field and could not be relied upon. That the lowest value of the cost function is achieved in the third case, as described above, does not imply that it is the preferred solution.

ICV is capable of determining the optimum mapping (velocity) field to a resolution greater than the number of intersections. However, in these image data, the first set of intersections is by straight lines (zero initial time delay). This introduces a non-uniqueness into the mapping of the intersecting line segments and does not permit this ICV feature to be used (cf the ‘aperture problem’ in section 13.2.2 of [28]). OTV image pairs generated at successive times in the same flow realization, e.g. for $t_1 > 0$ and $t_2 = t_1 + \tau$, would partially obviate this difficulty.

A second issue is that, in addition to being convected, OTV markers also diffuse. If the velocity field representation is allowed a higher spatial resolution, i.e. a large number of patches of extent comparable to the diffusive broadening of the marker lines (cf figures 9(a) and (b)), the cost function could be further minimized. This, however, would introduce a local divergence in the inferred velocity field, not owing to convection.

Finally, a finite signal-to-noise ratio, in the presence of high spatial resolution in the inferred field (a large number of patches and/or high-order B -spline basis functions), can introduce additional spurious features [26]. Unwarranted degrees of freedom in the variational problem will allow ICV to chase image noise to further minimize the cost function. This is analogous to selecting PIV cross-correlation patches that are too small in the presence of image noise.

2.5. Test facility issues of OTV

To determine the applicability of the OTV method to the pressure and temperature conditions of jet engine testing facilities, we have superimposed selected conditions of interest for aeromechanical aspects of engine testing [29] onto our results for the ozone number density calculations from the chemical kinetic calculations using the SENKIN code. In figure 11, contours of constant ozone concentration are plotted for various temperature and pressure air inlet

conditions. The two static temperature–pressure envelopes correspond to engine inlet Mach numbers of 0.3 and 0.65. The OTV demonstration point corresponds to standard atmospheric conditions used in obtaining the OTV images shown in figures 8 and 9. Most aeromechanical test conditions will result in higher concentrations of ozone than that at the OTV demonstration point. In the worst case, the ozone concentration will be reduced by about 50% from that at the OTV demonstration point. Thus substantial ozone concentrations are expected under the conditions of aeromechanical testing of jet engines.

An important issue in the application of the OTV method to large-scale facility tests is the degree of attenuation of the writing laser beams. At standard temperature and pressure, absorption of the 193 nm laser light by ambient molecular oxygen is a serious concern. An analytical investigation into the optimum wavelength for writing the tagged line was used to arrive at a procedure for minimizing beam delivery absorption due to O_2 outside the probe region as a function of propagation distance through ambient air.

Owing to the strong attenuation from ambient O_2 , especially over large distances, there may be some situations in which tuning the laser to the line centre is not advisable and a better approach would be to tune off the central absorption maximum. As an illustrative example, we chose to examine laser absorption and production of ozone signal in the vicinity of the P(15) line and as functions of position along a 360 cm propagation path. A 360 cm path length is typical of the diameter of a gas turbine engine testing facility. The P(15) feature was chosen because of its relative strength and proximity to the maximum gain curve for ArF. The feature was modelled with a Lorentzian broadened lineshape of 6.7 cm^{-1} FWHM. The partially resolved doublet lineshape feature is a result of the blended nature of the P(15) line with the adjacent R(17) line at 51168.9 cm^{-1} with the adjacent R(17) line at 51175.52 cm^{-1} [30]. To arrive at the effective absorptivity that the laser would experience at any given wavelength [25], the doublet was convoluted with a Gaussian broadened laser lineshape of 0.81 cm^{-1} FWHM, the linewidth of the narrowband ArF excimer laser. Given the absorptivity of oxygen as a function of wavelength, we can estimate the laser intensity for any wavelength at any

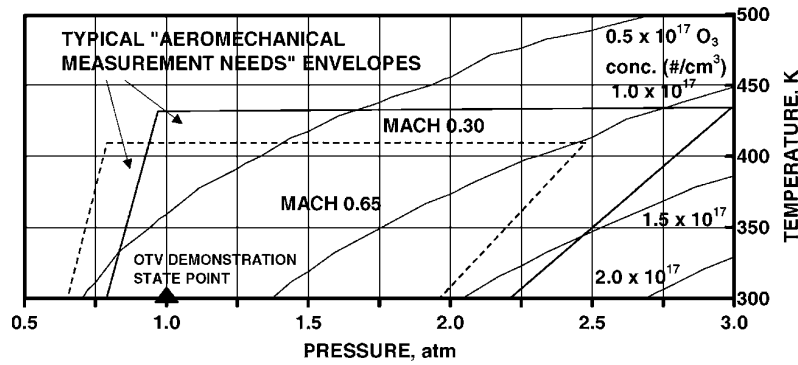


Figure 11. Ozone (O_3) concentration (number density cm^{-3}) versus temperature and pressure for various aeromechanical wind tunnel conditions.

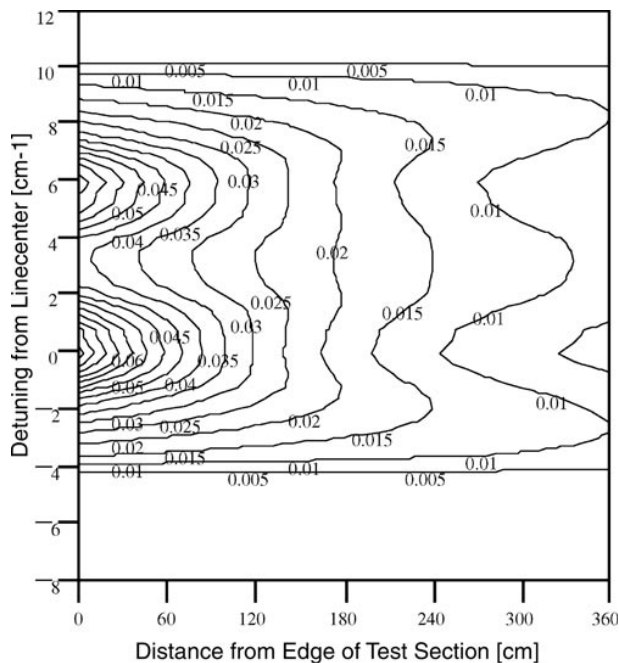


Figure 12. A contour plot of ozone production for a 10 cm probe volume following the traverse of a beam from the edge of the test section. Ozone production is plotted for each laser frequency detuned from the P(15) line.

point along the propagation path. This in turn allows us to estimate the O_3 produced. The amount of O_3 created is directly proportional to the loss of UV intensity over the probe region due to absorption by O_2 . For this calculation, a 10 cm long probe region was chosen.

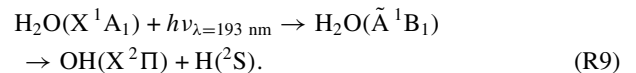
Our analysis calculates, for each frequency and distance from the edge of a test section, the amount of light lost over the following 10 cm long probe volume. In regions close to the edge of the theoretical test section, the highest flux of photons to the probe volume is delivered by tuning to the maximum absorption, i.e. the centre of the P(15) line. As the distance to the probe volume increases, however, the amount of light lost before reaching the probe volume becomes too high and it becomes more advantageous to tune off the maximum absorbance (or tune to a less absorbing feature). The contour plot of figure 12 serves as a guide for laser tuning as a function of path length to the probe volume. The centre of the P(15) line is shown at 0 cm^{-1} and the R(17)

line is at about 6 cm^{-1} . Our analysis indicates that, at large propagation distances ($\approx 170 \text{ cm}$ or greater), tuning the laser off the peak absorption at the line centres of P(15) and R(17) has a beneficial effect.

3. HTV

3.1. HTV photochemistry

HTV produces an OH molecular tag that persists in hot combustion products. The read and write steps use the same excimer lasers as those for OTV and the experimental set-up is the same as that shown in figure 7. Since HTV is amenable to use in high-temperature flows in which OTV does not work, the two methods complement each other. In HTV, an ArF excimer laser beam is focused into hot exhaust products and the water vapour is photodissociated by a single photon of 193 nm laser radiation to ‘write’ a grid of hydroxyl lines:



In the ‘read’ step, a light sheet from a KrF laser excites the OH to fluorescence by invoking the $A^2\Sigma^+ - X^2\Pi(3 \leftarrow 0)$ OH transition. Several ($3 \leftarrow 0$) rotational transitions are within the tuning range of the KrF laser [31]. The P₁(8) transition is used here. The fluorescence from the OH is recorded by an ICCD camera. The original and displaced images of the OH grid are recorded to determine the velocity field.

For significant photodissociation by reaction (R9), the water vapour must be vibrationally hot, as can be seen in the energy level diagram for H_2O shown in figure 13. The first absorption band for H_2O has a high-wavelength cut-off at $\approx 185 \text{ nm}$ for low-temperature (atmospheric conditions) H_2O [32]. Here the vibrational level of H_2O is designated by the term (v_s, v_b, v_a), that denotes the vibrational quantum numbers for the symmetrical stretch, symmetrical bend and asymmetrical stretch, respectively. For water vapour in the ground state (0, 0, 0), a single photon of 193 nm radiation has insufficient energy to reach the upper predissociative state, \tilde{A}^1B_1 .

The fraction of H_2O dissociated can be calculated in the limit of weak absorption ($\sigma_i n_i L < 1$) and is given by

$$\frac{n_{d_i}}{n_i} = \frac{\sigma_i E}{h\nu A}. \quad (4)$$

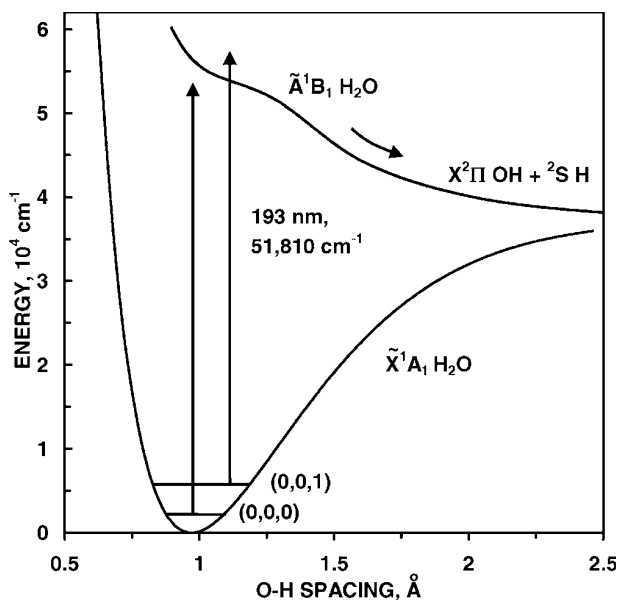


Figure 13. The energy-level diagram for H₂O. Ground-state data are from [38]; excited-state data are from [39]. Both curves are for the equilibrium bond angle (104.5°) and equilibrium spacing for the second OH bond (0.97 Å).

In the i th vibrational level, n_i is the number density of water, n_{di} is the number density of dissociated water and σ_i is the absorption cross-section. Here, E is the laser pulse energy, h is Planck's constant, ν is the frequency of the light, L is the length of the H₂O laden region through which the laser beam travels and A is the area of the laser beam. At room temperature, all the H₂O molecules are in the ground state (0, 0, 0). For 193 nm, the ground-state absorption cross-section is small, 8×10^{-22} cm²†, and leads to about 1% dissociation of the water vapour in room air for typical conditions (10 mJ per pulse, 0.3 mm diameter laser beam, 14 J cm⁻² fluence). For typical room air conditions of 21 °C and 50% relative humidity, this would produce a number density of about 3×10^{15} OH cm⁻³. This level of OH is difficult to detect by pumping the (3, 0) band of OH with a 248 nm KrF excimer laser [33] but could easily be seen pumping the (0, 0) band of OH with a 308 nm XeCl excimer laser.

The 193 nm H₂O absorption cross-sections for excited vibrational states are much larger than the ground-state cross-section. The enhanced absorption strength of vibrationally excited H₂O has been used to study photodissociation dynamics of particular ro-vibrational levels through IR–UV pump–probe experiments [34]. The excited vibrational state absorption cross-sections for the five lowest vibrational levels have recently been calculated by van Hemert and van Harrevelt (private communication). They used three-dimensional wavepacket calculations [35] that employ an \tilde{X}^1A_1 ground state potential surface [36] fitted to experimental data and an *ab initio* \tilde{A}^1B_1 excited state surface. These calculations assume that the H₂O is rotationally cold ($J'' = 0$) and they predict that about 98% of the OH photoproduct is in the vibrational ground state. Compared with the H₂O ground-state absorption cross-section of $8 \times$

† Private communication from M S van Hemert and R van Harrevelt (1999).

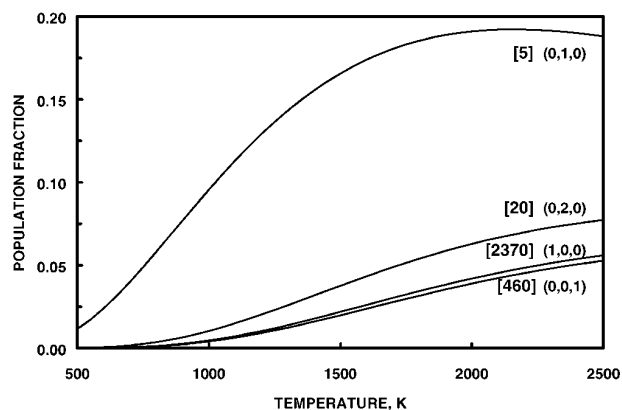


Figure 14. Equilibrium population fractions for vibrational levels of H₂O versus temperature for the first four vibrationally excited levels. Excited-state cross-section factors are shown in square brackets for each corresponding energy level of H₂O.

10^{-22} cm², the excited-state cross-sections are greater by factors of 5 (0, 1, 0), 20 (0, 2, 0), 460 (0, 0, 1) and 2370 (1, 0, 0)†. The vibrational levels (0, 0, 1) and (1, 0, 0) have strong absorptions and all the molecules in these levels will be dissociated under typical laser conditions (10 mJ per pulse for 0.3 mm diameter laser beam) according to equation (2). The other two levels, (0, 2, 0) and (0, 1, 0), will have dissociation fractions of 0.22 and 0.055, respectively.

Only at high temperatures will the excited vibrational levels have significant population fractions. The population fractions for the four lowest excited vibrational states are shown in figure 14 as functions of temperature. In H₂–air combustion hot products ($\phi = 0.69$, 2000 K, 25% H₂O), photodissociation of H₂O by a 193 nm laser (10 mJ, 0.3 mm diameter beam) will produce an estimated number density of 10^{17} OH cm⁻³. This is about 30 times higher than the number density of OH expected from humid room air.

3.2. Formation and destruction of HTV tags

The OH tag in HTV is formed immediately by 193 nm photodissociation (R9). The formation time is limited only by the excimer laser pulse width, which is ≈ 20 ns. This short formation time makes HTV amenable to use in high-speed flows, in which the times between ‘read’ and ‘write’ lasers may be less than 1 μ s.

The OH tag lifetime may be short or long depending upon the chemical environment. Under fuel rich conditions, the excess fuel will consume OH. To determine the lifetime of the OH tag in the hydrogen–air combustion hot products, the SENKIN chemical kinetic solver was used to calculate the chemical composition as a function of time [24] under constant enthalpy and pressure conditions. These conditions would be typical of those encountered in the atmosphere or in testing facilities. Here we use the CHEMKIN library and a shortened hydrogen–air combustion mechanism from GRIMECH 2.11 that consisted of 69 reactions. Since the calculations are for a carbon-free environment, reactions involving carbon are not considered.

The results of the SENKIN calculations for photodissociation of H₂O in lean and rich streams of H₂–air combustion

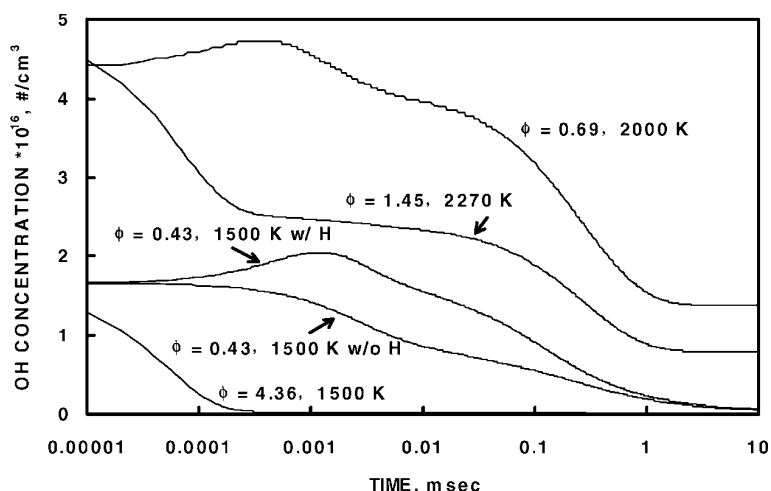


Figure 15. OH concentration versus time for four H₂–air post-flame flows, initially including OH and H photoproducts of the photodissociation of H₂O. The $\phi = 0.43$ flame was modelled both with (w/ H) and without (w/o H) H photoproduct.

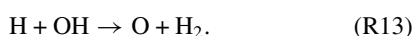
products are shown in figure 15. Here we have assumed that the initial amount of H₂O photodissociated is equal to the H₂O population in the (0, 0, 1) level. As discussed earlier, this level will be completely photodissociated by a typical laser beam (10 mJ, 0.3 mm diameter). This initial population is a conservative estimate. The (1, 0, 0) level will also be completely photodissociated. Considering all the vibrational levels, we are assuming about one third of the expected photodissociation of H₂O. Note that the original OH concentrations shown in figure 15 are the sums of the OH resulting from direct photodissociation (reaction (R9)) and the equilibrium concentration of OH. For times longer than 10 ms, the OH recombines to its equilibrium concentration.

For both of the lean flames ($\phi = 0.43$ and 0.69), the OH tag is produced in 20 ns and lasts for nearly 1 ms. Thus, in lean flames, HTV is appropriate for very high-speed to low-speed flows. In the lean flames, the OH concentration is enhanced over the amount initially produced by photodissociation. The OH concentration increases from the occurrence of photodissociation to about 1 μ s thereafter. According to analysis of the rates of production of OH [18], this increase in OH is due to two reactions:



In both cases, the H atoms produced in the original photodissociation step are converted to additional OH. This is confirmed by a calculation for lean H₂–air combustion products ($\phi = 0.43$) in which the initial H atom concentration was set to zero. As can be seen in figure 15, there is no increase in OH concentration when the H atoms are absent.

For lean flames, the two main reactions for destroying OH are [18]



In moderately rich flames ($\phi = 1.45$), the OH tag also persists for a long time, up to 1 ms, allowing HTV measurements over a wide range of low- and high-velocity flows. At $\phi = 1.45$

the main channel for destruction of OH is the reaction with excess H₂ fuel:



It can be seen that HTV works quite well both under moderately lean and under rich flame conditions. However, for very rich mixtures ($\phi = 4.36$), the excess fuel rapidly consumes the OH by reaction (R14) and the OH tag lasts only for about 0.1 μ s (figure 15).

3.3. HTV multi-line imaging

The same two narrowband lasers, ICCD camera, camera lens and camera filter are used both in the HTV and in the OTV set-up as shown previously in the multi-line experimental sketch in figure 7. Here, a Schott WG305 2 mm thick filter rejects unwanted scattered UV light. This is the same filter as that used in recording the 3×3 OTV images shown in figure 9. Thus OTV and HTV methods are complementary and can be used in flames to measure velocities in low-temperature air and high-temperature combustion.

In the HTV work, the ArF narrowband laser beam is split into additional beams to give more crossing points in the grid pattern. Using dielectric beam splitters and mirrors, a 3×4 grid is formed. In addition, one of the beams is retro-reflected to form the final 3×5 HTV grid shown in figure 16. A 500 mm lens focuses each ArF beam (≈ 10 mJ per beam) to a 0.3 mm diameter.

The HTV measurements shown in figure 16 were made in the post-flame zone of a lean ($\phi = 0.41$, 1450 K, 135 slpm total flowrate) H₂–air flame. The flame is produced by a 12.5 mm diameter ‘Hencken’ burner nozzle. The 12.5 mm exit of the ‘Hencken’ burner is a matrix of separate fuel and air tubes that form an array of small diffusion flames that quickly combine into a uniform stream of adiabatic combustion products. The flow is proceeding from the lower right-hand corner to the upper left-hand corner in each image. Measurements were performed at a location 20–25 diameters downstream of the nozzle’s exit. The velocity vectors shown in figure 16(a) are the result of the grid displacement over

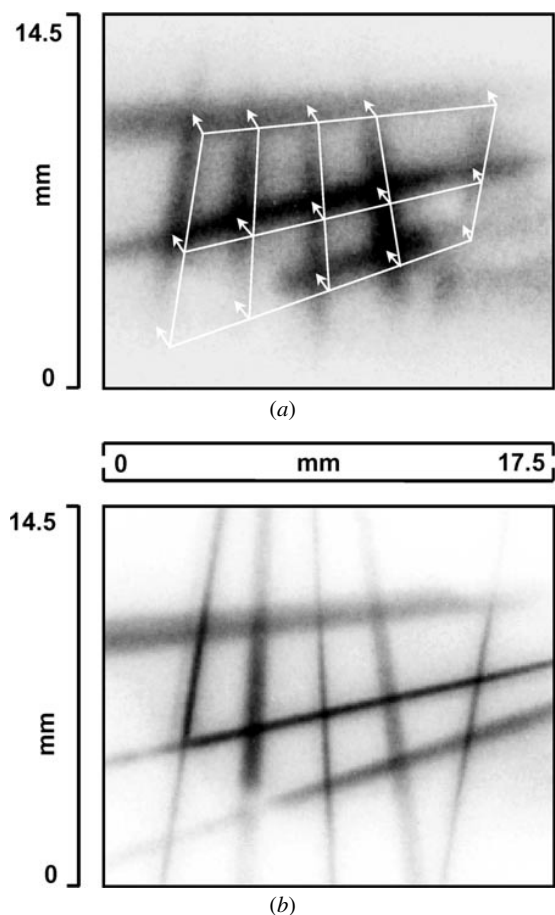


Figure 16. Single-pulse OH fluorescence images of a 3×5 HTV grid from hot photodissociation of H_2O , taken in the post-flame zone of a lean ($\phi = 0.41$, $T = 1450$ K) H_2 -air flame from a Hencken burner. Write/read delays are (a) $20 \mu\text{s}$ and (b) $0 \mu\text{s}$.

$\tau = 20 \mu\text{s}$. For the 1.5 mm tag lines' displacement, the velocity is about 75 m s^{-1} .

As can be seen in figure 16, the lines of OH diffuse rapidly in the high-temperature gases. The OH lines diffuse as [37]

$$w = [8 \ln(2) \tau D + w_0^2]^{1/2} \quad (5)$$

where w is the tag line width after a delay time τ , w_0 is the initial tag line width and D is an appropriate diffusion coefficient. Estimating D at $4.5 \text{ cm}^2 \text{ s}^{-1}$, the binary diffusion coefficient for motion of OH into N_2 at 1450 K (the adiabatic flame temperature for this H_2 -air flowfield) gives an expected tag line width of ≈ 0.37 mm. This assumes that w_0 is 0.3 mm, which is typical for lenses of focal length 500 mm at 193 nm. The average w in figure 16(a) is significantly larger than 0.37 mm, being closer to 1.2 mm. This could be at least partially explained by invoking the additional formation of OH by the H photoproduct. Before H reacts to form OH, it diffuses from the tag line at a faster rate than does the heavier OH molecule. The binary diffusion coefficient for motion of H into N_2 is about $17.8 \text{ cm}^2 \text{ s}^{-1}$ and as a result the tag line width is predicted to be about 0.53 mm.

In high-speed flows, the time between the writing and reading of the grid can be greatly reduced and will limit the diffusional broadening of lines in the grid. Thus a

prime application of HTV is to the high-temperature, high-speed environments found in aer propulsion, especially in supersonic ramjets.

4. Summary and conclusions

In this work, the same narrowband laser system is used for molecular flow tagging both in low- and in high-temperature flowfields. In low-temperature air flows measured using OTV, an ArF excimer laser produces a grid of O_3 molecules that is displaced by the flowfield and imaged by a KrF excimer laser sheet. In high-temperature combustion flows measured using HTV, the ArF laser produces a grid of hydroxyl molecules that is displaced by the flowfield and imaged by a KrF laser. In both cases, the ArF laser produces the molecular grid via a single-photon process that allows the creation of very long lines. Multi-line grids are used to demonstrate the feasibility of multipoint velocity measurements in room temperature flows (using OTV) and in high-temperature reacting flows (using HTV). The OTV grid images are analysed with ICV to give the velocity vector field. These two flow tagging techniques are complementary in that they provide velocity measurements in high- and low-temperature flows simultaneously since they both use the same laser system, which consists of tunable ArF and KrF lasers. Simultaneous use of HTV and OTV allows interrogation of reacting flowfields both in unreacted, cold regions (without hot H_2O) and in reacted, hot regions (where thermal decomposition of O_3 is problematic), allowing velocimetry in all regions of a combustion flowfield.

Acknowledgments

The Vanderbilt University authors gratefully acknowledge the support of NASA-Glenn (grant NAG3-1984, with Dr Richard G Seasholtz as the technical monitor) and BMDO-ARO (DURIP award DAAG55-98-1-0197 with Dr David M Mann as the technical monitor). The Vanderbilt University and MetroLaser authors wish to acknowledge the support of the Arnold Engineering Development Center (DoD SBIR Phase II grant F40600-96-C-0002, with Dr Ronald H Kohl and Dr H Thomas Bentley as technical monitors). We thank Dr Richard Yetter of Princeton University for providing us with his O_3 chemistry reaction mechanism and thank S Nandula for technical assistance. The Cal Tech authors gratefully acknowledge the support of AFOSR (grant F49620-98-1-0052 with Dr Julian Tishkoff as the technical monitor).

References

- [1] Drain L E 1980 *The Laser Doppler Technique* (New York: Wiley)
- [2] Adrian R J 1991 Particle-imaging techniques for experimental fluid mechanics *Ann. Rev. Fluid Mech.* **23** 261–304
- [3] Measures R M 1968 Selective excitation spectroscopy and some possible applications *J. Appl. Phys.* **39** 5232–45
- [4] Zimmermann M and Miles R B 1980 Hypersonic-helium-flow-field measurements with the resonant Doppler velocimeter *Appl. Phys. Lett.* **37** 885–7

- [5] McDaniel J C, Hiller B and Hanson R K 1983 Simultaneous multiple-point velocity measurements using laser-induced iodine fluorescence *Opt. Lett.* **8** 51–3
- [6] Paul P H, Lee M P and Hanson R K 1989 Molecular velocity imaging of supersonic flows using pulsed planar laser-induced fluorescence of NO *Opt. Lett.* **14** 417–19
- [7] Seasholtz R G, Zupanc F J and Schneider S J 1992 Spectrally resolved Rayleigh scattering diagnostic for hydrogen–oxygen rocket plume studies *J. Prop. Power* **8** 935–42
- [8] Forkey J N, Finkelstein N D, Lempert W R and Miles R B 1996 Demonstration and characterization of filtered Rayleigh scattering for planar velocity measurements *AIAA J.* **34** 442–8
- [9] Hiller B, Booman R A, Hassa C and Hanson R K 1984 Velocity visualization in gas flows using laser-induced phosphorescence of biacetyl *Rev. Sci. Instrum.* **55** 1964–7
- [10] Stier B and Koochesfahani M M 1999 Molecular tagging velocimetry (MTV) measurements in gas phase flows *Exp. Fluids* **26** 297–304
- [11] Orlemann C, Schulz C and Wolfrum J 1999 NO-flow tagging by photodissociation of NO₂. A new approach for measuring small-scale flow structures *Chem. Phys. Lett.* **307** 15–20
- [12] Boedecker L R 1989 Velocity measurement by H₂O photolysis and laser-induced fluorescence of OH *Opt. Lett.* **14** 473–5
- [13] Noullez A, Wallace G, Lempert W, Miles R B and Frisch U 1997 Transverse velocity increments in turbulent flow using the RELIEF technique *J. Fluid Mech.* **339** 287–307
- [14] Pitz R W, Brown T M, Nandula S P, Skaggs P A, DeBarber P A, Brown M S and Segall J 1996 Unseeded velocity measurement by ozone tagging velocimetry *Opt. Lett.* **21** 755–7
- [15] Pitz R W, Ribarov L A, Wehrmeyer J A, Batliwala F and DeBarber P A 1998 Ozone tagging velocimetry for unseeded velocity measurements in air flows *20th AIAA Advanced Measurement and Ground Testing Technology Conf.*
- [16] Ribarov L A, Wehrmeyer J A, Batliwala F, Pitz R W and DeBarber P A 1999 Ozone flow tagging velocimetry using narrowband excimer lasers *AIAA J.* **37** 708–14
- [17] Wehrmeyer J A, Ribarov L A, Oguss D A, Batliwala F, Pitz R W and DeBarber P A 1999 Flow tagging velocimetry for low and high temperature flowfields *37th AIAA Aerospace Sciences Meeting*
- [18] Wehrmeyer J A, Ribarov L A, Oguss D A and Pitz R W 1999 Flame flow tagging velocimetry with 193 nm H₂O photodissociation *Appl. Opt.* **38** 6912–17
- [19] Tokumaru P T and Dimotakis P E 1995 Image correlation velocimetry *Exp. Fluids* **19** 1–15
- [20] Freisinger B, Kogelschatz U, Schäfer J H, Uhlenbusch J and Viöl W 1989 Ozone production in oxygen by means of F₂-laser irradiation at $\lambda = 157.6$ nm *Appl. Phys. B* **49** 121–9
- [21] Finlayson-Pitts B J and Pitts J N Jr 1986 *Atmospheric Chemistry: Fundamentals and Experimental Techniques* (New York: Wiley–Interscience)
- [22] Greenblatt G D and Wiesenfeld J R 1983 Time-resolved resonance fluorescence studies of O(¹D₂) yields in the photodissociation of O₃ at 248 nm and 308 nm *J. Chem. Phys.* **78** 4924–8
- [23] Park H and Slanger T G 1994 O₂ (X, $v = 8$ –22) 300 K quenching rate coefficients for O₂ and N₂, and O₂ (x) vibrational distribution from 248 nm O₃ photodissociation *J. Chem. Phys.* **100** 287–300
- [24] Lutz A E, Kee R J and Miller J A 1988 *SENKIN: A Fortran Program for Predicting Homogeneous Gas Phase Chemical Kinetics with Sensitivity Analysis* (Livermore, CA: Sandia National Laboratories)
- [25] Lee M 1991 Temperature measurements in gases using planar laser-induced fluorescence imaging of NO and O₂ *PhD Thesis* Mechanical Engineering Department, Stanford University
- [26] Gornowicz G G 1997 Continuous-field image correlation velocimetry and its application to unsteady flow over an airfoil *Engineer Thesis* Graduate Aeronautical Laboratories, California Institute of Technology
- [27] Piegl L and Tiller W 1995 *The NURBS Book* (Berlin: Springer)
- [28] Jähne B 1997 *Digital Image Processing* 4th edn (Berlin: Springer)
- [29] Kohl R H and Grinstead J H 1998 RELIEF velocimetry measurements in the RID research facility at AEDC *20th AIAA Advanced Measurement and Ground Testing Technology Conf.*
- [30] Yoshino K, Freeman D E and Parkinson W H 1984 Atlas of the Schumann–Runge absorption bands of O₂ in the wavelength region 175–205 nm *J. Chem. Phys. Ref. Data* **13** 207–27
- [31] Andresen P, Bath A, Gröger W, Lülff H W, Meijer G and ter Meulen J J 1988 Laser-induced fluorescence with tunable excimer lasers as a possible method for instantaneous temperature field measurements at high pressures: checks with an atmospheric flame *Appl. Opt.* **27** 365–78
- [32] Watanabe K and Zelikoff M 1953 Absorption coefficients of water vapor in the vacuum ultraviolet *J. Opt. Soc. Am.* **43** 753–5
- [33] Cheng T S, Wehrmeyer J A, Pitz R W, Jarrett O Jr and Northam G B 1994 Raman measurement of mixing and finite-rate chemistry in a supersonic hydrogen–air diffusion flame *Combust. Flame* **99** 157–73
- [34] Häusler D, Andresen P and Schinke R 1987 State to state photodissociation of H₂O in the first absorption band *J. Chem. Phys.* **87** 3949–65
- [35] Kroes G-J, van Dishoeck E F, Beärda R A and van Hemert M C 1993 Photodissociation of CH₂. II. Three-dimensional wave packet calculations on dissociation through the first excited triplet state *J. Chem. Phys.* **99** 228–36
- [36] Polyansky O L, Jensen P and Tennyson J 1996 The potential energy surface of H₂¹⁶O *J. Chem. Phys.* **105** 6490–7
- [37] Miles R, Lempert W and Zhang B 1991 Turbulent structure measurements by RELIEF flow tagging *Fluid Dyn. Res.* **8** 9–17
- [38] Sorbie K S and Murrell J N 1976 Theoretical study of the O(¹D) + H₂(¹Σ_g⁺) reactive quenching process *Mol. Phys.* **31** 905–20
- [39] Staemmler V and Palma A 1985 CEPA calculations of potential energy surfaces for open-shell systems. IV. Photodissociation of H₂O in the \tilde{A}^1B_1 state *Chem. Phys.* **93** 63–9